Vlasov-Poisson simulations of electrostatic parametric instability for localized Langmuir wave packets in the solar wind

Pierre Henri, Francesco Califano, Carine Briand, André Mangeney

JOURNAL OF GEOPHYSICAL RESEARCH, VOL. 115, A06106, doi:10.1029/2009JA014969, 2010

Vlasov-Poisson simulations of electrostatic parametric instability for localized Langmuir wave packets in the solar wind

P. Henri,[1,2] F. Califano,[1,2] C. Briand,[3] and A. Mangeney[3]

Received 7 October 2009; revised 2 December 2009; accepted 12 January 2010; published 18 June 2010.

[1] Recent observation of large-amplitude Langmuir waveforms during a type III event in the solar wind has been interpreted as the signature of the electrostatic decay of beam-driven Langmuir waves. This mechanism is thought to be a first step to explain the generation of type III radio emission. The threshold for this parametric instability in the typical solar wind condition has been investigated through 1D-1V Vlasov-Poisson simulations. We show that the amplitude of the observed Langmuir beatlike waveforms is of the order of the effective threshold computed from the simulations. The expected levels of associated ion acoustic density fluctuations have also been computed for comparison with observations.

Citation: Henri, P., F. Califano, C. Briand, and A. Mangeney (2010), Vlasov-Poisson simulations of electrostatic parametric instability for localized Langmuir wave packets in the solar wind, *J. Geophys. Res.*, *115*, A06106, doi:10.1029/2009JA014969.

1. Introduction

[2] During a solar flare, high-energy electrons (1–100 keV) are expelled from the solar corona and travel along the interplanetary magnetic field lines, producing a bump on the local electron distribution function. Langmuir waves then grow via the so-called bump-on-tail instability. Langmuir waves are observed at amplitude large enough ($E^2/(8\pi nT) \simeq 10^{-3}$–$10^{-4}$) to further excite electromagnetic waves through nonlinear processes. These electromagnetic waves are the main signature of type III radio bursts. Wave-wave interaction through parametric instabilities have been shown to be the physical mechanism underlying the non linear evolution of large amplitude Langmuir waves.

[3] Langmuir electrostatic decay (LED), also called Langmuir decay instability (LDI) or parametric decay instability (PDI) in the literature, enables energy transfer from a finite amplitude Langmuir wave L toward a second Langmuir wave L' and an ion acoustic wave (IAW) S through a three-wave resonant interaction:

$$L \rightarrow L' + S.$$

This process is thought to be a first step toward the generation of solar wind type III radio emission at twice the plasma frequency ($T_{2f_{pe}}$), as a result of a coalescence of the two Langmuir waves [*Ginzburg and Zheleznyakov*, 1958]:

$$L + L' \rightarrow T_{2f_{pe}}.$$

[4] Spectral observations of high-frequency intense Langmuir waves and low-frequency ion acoustic waves during type III bursts have been interpreted as a signature of Langmuir electrostatic decay [*Lin et al.*, 1986a]. Furthermore, waveform observations during type III bursts of modulated Langmuir wave packets on one hand [*Cairns and Robinson*, 1992; *Hospodarsky and Gurnett*, 1995; *Bale et al.*, 1996; *Li et al.*, 2003] and of IAW frequency drift associated with type III electron beam velocity drift on the other hand [*Cairns and Robinson*, 1995] have both been interpreted by the Langmuir electrostatic decay.

[5] The LED is a resonant parametric instability. To be resonant, the three-wave coupling requires the fundamental equations of energy and momentum conservation to be satisfied:

$$\omega_L = \omega_{L'} + \omega_S \qquad \vec{k}_L = \vec{k}_{L'} + \vec{k}_S, \tag{1}$$

where ω and $\vec{k}$ are the frequency and wave number of the waves. Moreover, for the LED to develop, the electric field of the mother Langmuir wave has to reach a critical value. The analytical calculation of this threshold has been discussed by *Nishikawa* [1968], *Sagdeev and Galeev* [1969], *Dysthe and Franklin* [1970], *Bardwell and Goldman* [1976], and *Robinson et al.* [1993] by considering three monochromatic waves. The underlying idea is that for the instability to develop, the growth rate γ_{LED} of the two product waves must be higher than their own linear Landau damping rates $\gamma_{L'}$ and γ_S:

$$\gamma_{\mathrm{LED}} > \sqrt{\gamma_{L'}\gamma_S}.$$

[1]Dipartimento Fisica, Università di Pisa, Pisa, Italy.
[2]Also at Laboratoire d'Études Spatiales et d'Instrumentation en Astrophysique, Observatoire de Paris, Université Pierre et Marie Curie, Université Paris Diderot, CNRS, Meudon, France.
[3]Laboratoire d'Études Spatiales et d'Instrumentation en Astrophysique, Observatoire de Paris, Université Pierre et Marie Curie, Université Paris Diderot, CNRS, Meudon, France.

0148-0227/10/2009JA014969

The threshold for parametric decay of the mother Langmuir wave is thus evaluated in term of the electric to kinetic energy ratio [*Bardwell and Goldman*, 1976]:

$$\frac{\epsilon_0 E^2}{n k_B T} > 8 \frac{\gamma_{L'}}{\omega_{L'}} \frac{\gamma_S}{\omega_S},$$

with $\omega_{L'}$, ω_S the angular frequency of the daughter waves. The threshold for electrostatic decay has been estimated for typical solar wind parameters to be $(\epsilon_0 E^2)/(n k_B T) \geq 2.5 \times 10^{-5}$ [*Lin et al.*, 1986b]. To our knowledge, only LED that couples three monochromatic waves have been considered analytically. Indeed, the analytical treatment of resonance becomes complicated when considering a finite frequency bandwidth, in which case a numerical treatment is necessary.

[6] Earlier related works on simulations of LED have been based on the Zakharov equations [*Sprague and Fejer*, 1995; *Gibson et al.*, 1995; *Soucek et al.*, 2003], considering the instability as a fluid mechanism. Recently, kinetic simulations using PIC codes [*Matsukiyo et al.*, 2004; *Huang and Huang*, 2008] and Vlasov codes [*Goldman et al.*, 1996; *Umeda and Ito*, 2008] have shown that the beam-plasma interaction can saturate through LED and have been able to reproduce the modulated shape of Langmuir waves.

[7] If the threshold for LED is commonly thought to be at moderate amplitude, a recent numerical work [*Umeda and Ito*, 2008] claims that no LED would occur until the electric energy is comparable to the plasma kinetic energy. As a result, it would be no more possible to consider the LED as a mechanism for the generation of type III radio emission.

[8] *Henri et al.* [2009] (hereinafter referred to as Paper I) recently reported direct observations of Langmuir waves decaying into secondary Langmuir waves and acoustic waves during a type III solar event, from STEREO/WAVES data. They found that the Doppler-shifted frequencies of the three observed waves satisfy the resonant relations of momentum and energy conservation expected for three-wave coupling. A bicoherence analysis confirmed the phase coherence of the three waves. In this former work, the LED threshold and the growth rate of IAW density fluctuations generated by LED were both evaluated from analytical solutions involving a purely monochromatic three-wave coupling [*Sagdeev and Galeev*, 1969]. However, observations show that (1) the large amplitude Langmuir waves are isolated wave packets with a packet width of the order of a few wavelengths and (2) ion and electron temperatures are close ($0.1 < T_e/T_i < 10$) so that ion acoustic waves associated with the LED should be Landau damped. Thus several questions remain open about the generation and the dynamics of the LED observed in the solar wind: (1) What are the threshold and the growth rate of the LED when electron and ion temperatures are close? What is the effective threshold of LED when the mother Langmuir wave is a localized wave packet? (2) What is the saturation level for IAW density fluctuations in these conditions? What is the expected level of IAW density fluctuations where saturation is not observed? The goal of this paper is to answer these questions by studying the dynamics of the LED through 1D-1V Vlasov-Poisson simulations.

[9] The paper is organized as follows. The Vlasov-Poisson simulation model is described in section 2. The numerical results are presented in section 3, first for a monochromatic mother Langmuir wave (section 3.1), then for a mother Langmuir wave packet (section 3.2). Growth rates, saturation levels for IAW density fluctuations and threshold for LED are studied. The simulation results are finally discussed in section 4 in the context of solar wind observations. Particular attention is paid to the case of equal temperature for electrons and ions, in which case the growth of IAW should be limited by its Landau damping.

2. Full Vlasov-Poisson Simulation Model

[10] In typical solar wind conditions, the ratio between electron and ion temperatures fluctuates around 1. The IAW produced during three-wave coupling should then be suppressed by Landau damping. This would limit the development of the IAW and thus the LED. However, the IAW Landau damping rate in such temperature condition cannot be solved analytically, so that it cannot be included in a fluid code. Kinetic effects due to wave-particle interactions are to be taken into account self-consistently as a possible limitation for the instability to grow. A Vlasov-Poisson approach has thus been used to study LED dynamics. It allows to consider self-consistently the decay of the Langmuir wave together with damping effect on the product waves. Since solar wind electrons are weakly magnetized ($\omega_{ce}/\omega_{pe} \simeq 10^{-2}$), magnetic effects are discarded.

[11] The Vlasov-Poisson system is solved for the electron and ion distribution function, $f_e(x, v, t)$ and $f_i(x, u, t)$, with the numerical scheme described by *Mangeney et al.* [2002], limiting our study to the 1D-1V case. The equations are normalized by using the following characteristic electron quantities: the charge e, the electron mass m_e, the electron density n_e, the plasma (angular) frequency $\omega_{pe} = \sqrt{4\pi n_e e^2/m_e}$, the Debye length $\lambda_D = \sqrt{T_e/4\pi n_e e^2}$, the electron thermal velocity $v_{\mathrm{th},e} = \lambda_D \omega_{pe} = \sqrt{T_e/m_e}$ and an electric field $\overline{E} = m_e v_{\mathrm{th},e} \omega_{pe}/e$. Then, the dimensionless equations for each species read:

$$\frac{\partial f_e}{\partial t} + v \frac{\partial f_e}{\partial x} - (E + E_{\mathrm{ext}}^{\mathrm{init}}) \frac{\partial f_e}{\partial v} = 0, \tag{2}$$

$$\frac{\partial f_i}{\partial t} + u \frac{\partial f_i}{\partial x} + \frac{1}{\mu} (E + E_{\mathrm{ext}}^{\mathrm{noise}}) \frac{\partial f_i}{\partial u} = 0, \tag{3}$$

$$\frac{\partial^2 \phi}{\partial x^2} = \int f_e dv - \int f_i du; \qquad E = -\frac{\partial \phi}{\partial x}, \tag{4}$$

where v (u, respectively) is the electron (ion, respectively) velocity normalized to the electron thermal velocity. Here $\mu = m_i/m_e = 1836$ is the ion-to-electron mass ratio. ϕ and E are the self-consistent electric potential and electric field generated by the plasma charge density fluctuations according to Poisson equation (4). $E_{\mathrm{ext}}^{\mathrm{init}}$ and $E_{\mathrm{ext}}^{\mathrm{noise}}$ are "external" drivers added to the Vlasov equation that can be switched on or off during the run. The electron (ion, respectively) distribution function is discretized in space for $0 \leq x < L_x$, with $L_x = 5000\ \lambda_D$ the total box length, with a resolution of $dx = \lambda_D$. The electron velocity grid ranges over $-5\ v_{\mathrm{th},e} \leq v \leq +5\ v_{\mathrm{th},e}$, with a resolution of $dv = 0.04\ v_{\mathrm{th},e}$. ($-5\ u_{\mathrm{th},i} \leq u \leq +5\ u_{\mathrm{th},i}$, respectively, with a reso-

lution of $du = 0.04\ u_{\mathrm{th},i}$ for the ion velocity grid, where $u_{\mathrm{th},i}$ is the ion thermal velocity). Finally, periodic boundary conditions are used in the spatial direction.

[12] In all the runs the following initial conditions have been taken: electron and ion distributions functions are initially Maxwellian with respect to velocity, with a random noise in density:

$$f_e(x,v) = \frac{e^{-v^2}}{\sqrt{2\pi}}\left[1 + \epsilon \sum_k \cos(kx + \psi_k)\right] \tag{5}$$

$$f_i(x,u) = \frac{\sqrt{\frac{\Theta}{\mu}}e^{-\frac{\Theta}{\mu}u^2}}{\sqrt{2\pi}}\left[1 + \epsilon' \sum_k \cos(kx + \psi'_k)\right], \tag{6}$$

where $\Theta = T_i/T_e$ is the ion-to-electron temperature ratio set to $\Theta = 0.1$ or 1 in the different runs. Variables ψ_k and ψ'_k are random phases with a uniform distribution. The parameter ϵ (ϵ', respectively) is the amplitude of the initial electron (ion, respectively) density level of noise. The parameters (ϵ, ϵ') are chosen so that the development of the instability happens relatively rapidly, as Vlasov codes have a very low level of numerical noise. The influence of the level of initial density fluctuation on the LED has been studied for values $10^{-8} < \epsilon$, $\epsilon' < 10^{-4}$. Neither the growth rate of density fluctuations, nor its saturation level are modified by the choice of the parameters ϵ and ϵ', as long as they remain weak. Only the time needed for the instability to saturate is modified. The chosen values $\epsilon = \epsilon' = 10^{-5}$ are a good compromise to limit the computation time. However, when the electron and proton temperatures are of the same order the initial perturbation on ion density is rapidly damped out and the generation of the IAW starts from the numerical noise. When starting from a monochromatic Langmuir wave (section 3.1), the interaction time between the waves is "infinite." In this case the IAW can grow from the numerical noise to significant values providing we wait for long enough. On the other hand, when starting from a Langmuir wave packet (section 3.2) the interaction time between the waves is now finite. A continuous injection of noise is then needed to seed the instability. This is why an external driver $E_{\mathrm{ext}}^{\mathrm{noise}}$ is added in the Vlasov equation for ions (equation (3)). The aim is to control the generation of a continuous incoherent noise in the proton density. For self-consistency, the driver is used in both cases $\Theta = 0.1$ and $\Theta = 1$. The details of the forcing are described in appendix A. From a physical point of view, IAW grow from the proton density fluctuations background. Note that such density irregularities are observed in the solar wind [*Celnikier et al.*, 1987; *Harvey et al.*, 1988].

[13] In space conditions, the full physical process for the nonlinear evolution of large amplitude Langmuir waves is characterized by two successive steps. The first one is the generation of Langmuir waves from the bump-on-tail instability, the second one the electrostatic decay of these Langmuir waves if their amplitudes reach the LED threshold. Other authors have already studied the generation of beam driven Langmuir wave packets [*Omura et al.*, 1994, 1996; *Silin et al.*, 2007; *Umeda*, 2007]. Among their results, they have shown that the beam-driven Langmuir waves are localized packets. This localization is explained through the mechanism of kinetic localization in the framework of a nonlinear trapping theory [*Muschietti et al.*, 1995, 1996; *Akimoto et al.*, 1996; *Usui et al.*, 2005]. It is has also been shown that the beam-driven Langmuir wave packets are formed on time scales considerably shorter than those of parametric instabilities [*Intrator et al.*, 1984; *Akimoto et al.*, 1996].

[14] Our aim here is to focus the attention on the LED process. Motivated by the fact that the generation and localization of beam-driven Langmuir waves are decoupled from the LED process, we choose not to generate Langmuir waves by a bump-on-tail instability, but to resonantly grow the initial Langmuir wave by means of an electric field $E_{\mathrm{ext}}^{\mathrm{init}}$ added in equation (2). This method enables to have a direct control on the energy and the spectrum of the initial Langmuir wave and avoid other effects due to the non-Maxwellian character of the initial distribution function. Switched on at the beginning of the run, it acts as a driver to resonantly grow the wave with the desired spectrum and electric field amplitude. Details on the external driver $E_{\mathrm{ext}}^{\mathrm{init}}$ are given in Appendix B. The external driver is then switched off and the generated Langmuir wave evolves self-consistently. In section 3.1, a monochromatic Langmuir wave of wavelength λ_L and amplitude E_L is generated by imposing $E_{\mathrm{ext}}^{\mathrm{init}} = E_{\mathrm{ext}}^{(1)}$ (compare equation (B1)). In section 3.2, a Langmuir wave packet of mean wavelength λ_L, packet width Δ and maximum amplitude E_L is generated by imposing $E_{\mathrm{ext}}^{\mathrm{init}} = E_{\mathrm{ext}}^{(2)}$ (compare equation (B2)). The external electric field $E_{\mathrm{ext}}^{\mathrm{init}}$ is switched off when the amplitude (maximum amplitude, respectively) of the generated Langmuir wave (wave packet, respectively) reaches the desired value E_L. This happens typically for time $t < 300\ \omega_{pe}^{-1}$, small compared to the decay time scale. So, the resonant generation of the Langmuir wave (wave packet, respectively) does not interfere with the LED mechanism.

[15] In order to compare the simulation results with observations of electric waveforms during type III events, the Langmuir wavelength and amplitude are set as indicated by solar wind observations. Langmuir waves grow by resonance with an electron beam at phase velocity $v_L^{\Phi} = \omega_L/k_L \simeq V_{\mathrm{beam}}$. Typical electron beams span in the range 0.05–0.2 c [*Dulk et al.*, 1987; *Hoang et al.*, 1994]. Taking into account the Langmuir dispersion relation, we deduce Langmuir wavelengths in the range $\lambda_L = [100\text{–}600]\ \lambda_D$. However, for a temperature ratio $\Theta = 1$ ($\Theta = 0.1$, respectively), the daughter Langmuir wave packet is expected, from equation (1) and respective dispersion relations, to be backscattered for $\lambda_L < 285\ \lambda_D$ ($\lambda_L < 385\ \lambda_D$, respectively), and scattered forward for $\lambda_L > 285\ \lambda_D$ ($\lambda_L > 385\ \lambda_D$, respectively). Thereby, mother and daughter Langmuir Doppler-shifted frequencies are very close and hardly separated on observation. Thus, to be able to compare the simulations with observations, we choose Langmuir wavelengths that allow observations of LED, namely $\lambda_L = 100\ \lambda_D$ for the initial monochromatic Langmuir wave in section 3.1, and $50\ \lambda_D < \lambda_L < 400\ \lambda_D$ for the initial Langmuir wave packet in section 3.2. Since the phase velocities of the two expected Langmuir waves are large enough, their Landau damping can be neglected. Thus the phase velocity of the Langmuir waves do not need to be resolved in the electron distribution function velocity box. On the other hand, the expected IAW travel at the ion-sound speed $c_s = \sqrt{(T_e + T_i)/m_i}$, which is of the order of the ion thermal speed when electron and ion temperature are close,

Table 1. Expected Waves Involved in the Langmuir Electrostatic Decay, Given the Initial Langmuir Wavelength and Using Equations (1) for $\Theta = 0.1$ and $\Theta = 1$[a]

	Waves	Wavelength (λ_D)	Wave Number (λ_D^{-1})	Phase Velocity ($v_{th}^e = \lambda_D \omega_{pe}^{-1}$)	Group Velocity ($v_{th}^e = \lambda_D \omega_{pe}^{-1}$)
$\Theta = 0.1$	L	$\lambda_L = 100$	$k_L = 0.063$	$v_L^\phi = 16$	$v_L^g = 0.189$
	L'	$\lambda_{L'} = 132$	$k_{L'} = (-)\ 0.047$	$v_{L'}^\phi = -21$	$v_{L'}^g = -0.141$
	S	$\lambda_S = 57$	$k_S = 0.110$	$c_s = 0.024$	$c_s = 0.024$
$\Theta = 1$	L	$\lambda_L = 100$	$k_L = 0.063$	$v_L^\phi = 16$	$v_L^g = 0.189$
	L'	$\lambda_{L'} = 154$	$k_{L'} = (-)\ 0.041$	$v_{L'}^\phi = -24.5$	$v_{L'}^g = -0.123$
	S	$\lambda_S = 60$	$k_S = 0.104$	$c_s = 0.033$	$c_s = 0.033$

[a]The table shows for each wave the expected wavelength (in Debye length λ_D) corresponding wave number (in inverse Debye length λ_D^{-1}) used in the paper figures and phase and group velocities (in $\lambda_D \omega_{pe}^{-1}$).

thus leading to a large Landau damping. The ion-sound speed is resolved in the ion distribution function velocity box.

[16] The typical Langmuir waves amplitude is directly given by waveform observations and normalized to the electron temperature:

$$E = \sqrt{\frac{\epsilon_0 E_{\text{obs}}^2/2}{n k_b T_e}}. \tag{7}$$

In Paper I, the typical observed values are $10^{-2} < E_L < 10^{-1}$. We choose several amplitudes in the range $10^{-3} < E_L < 1$.

3. Numerical Results

[17] During the first part of the simulation ($0 < t < t_0$) the external electric pump generates a Langmuir monochromatic wave (wave packet, respectively) at the desired amplitude. At time $t = t_0$, the external pump is switch off when the Langmuir wave (wave packet, respectively) reaches the desired value. For $t > t_0$ the Langmuir wave evolves self-consistently. We consider time $t = t_0$ as the beginning of the numerical experiment.

[18] The typical intensity of the electric field of the IAW generated by LED is much below the level of Langmuir electric noise. In the following, the ion *density* is therefore used as a tracer for IAW.

3.1. Electrostatic Decay of a Monochromatic Langmuir Wave

[19] In this section, we consider the evolution of a monochromatic wave generated by the external pump defined in equation (B1). Table 1 summarizes the expected wavelength, wave numbers, phase velocity and group velocity in the case of three monochromatic resonant waves, as a function of the mother Langmuir wavelength λ_L and the temperature ratio Θ.

[20] A broad spectrum of daughter waves generated by the instability is clearly seen on Figure 1. It shows the electric field and ion density spectrum, black and red lines, respectively, at given times. Dashed vertical lines indicate the expected wave numbers of the LED products as reported in Table 1. In Figure 1 (top left), $t = 10^3\ \omega_{pe}^{-1}$, the spectrum corresponds to the "initial condition" where only the Langmuir wave at $k_L = 0.063\ \lambda_D^{-1}$ and its harmonic at $0.13\ \lambda_D^{-1}$ are present. Then, the growth of the LED produces (1) a daughter Langmuir waves L' at $k_{L'} \simeq 0.04\ \lambda_D^{-1}$ in the electric field spectrum and (2) an IAW at $k_S \simeq 0.10\ \lambda_D^{-1}$ in the ion density spectrum. Both are shown in Figure 1: $t = 5 \times 10^4\ \omega_{pe}^{-1}$ (Figure 1, top right) and $t = 10^5\ \omega_{pe}^{-1}$ (Figure 1, bottom left). Finally, at $t > 10^5$ (Figure 1, bottom right) harmonics of the IAW are produced, low-k fluctuations are generated and the LED saturates. We need to stress here that during the decay phase, even if the Langmuir wave L is monochromatic, the product waves L' and S are both wave packets with wave numbers centered on the expected wave number. This results from the fact that different k channels are available for energy transfer from the Langmuir wave toward its decay products. Indeed Figure 2 shows the linear growth rate versus k for different wave numbers of the daughter Langmuir wave electric field (in black) and IAW density fluctuations (in red) spectrum. Growth rates for both daughter waves are overplotted with k_S axis and $k_{L'}$ axis such that $k_S + k_{L'} = k_L$. As expected, the growth rates are the same for each couple of product waves that verify the wave number resonant condition. The spread in wave number is about $\Delta k_{L'} = \Delta k_S \simeq 0.025$ for both waves, thereby a relative spectral spread of $\Delta k_S/k_S \simeq 0.2$ for the IAW and $\Delta k_{L'}/k_{L'} \simeq 0.6$ for the Langmuir product wave. Note that the generation of a large spectrum of product waves limits the spatial coherence of the interaction. This point is discussed in section 4.2.

[21] We then compute an "integrated" (over space) ion density fluctuations $\langle \delta n \rangle$ generated by LED defined by

$$\langle \delta n \rangle(t) = \sqrt{\frac{1}{L_x} \int_0^{L_x} (n(t,x) - n_0)^2\, dx}, \tag{8}$$

with the mean ion density $n_0 = 1$ in dimensionless units. We define the saturation level δn_{sat} as the maximum value reached by the mean density fluctuations $\langle \delta n \rangle(t)$ during the simulation. The growth rate for average density fluctuation is here $\gamma_{\text{LED}} = 2.3 \times 10^{-5}\ \omega_{pe}$, or $\gamma_{\text{LED}} = 4.1 \times 10^{-2}\ f_S$ when expressed in term of the IAW frequency, defined by $f_S = c_s/\lambda_S = 5.5 \times 10^{-4}$. This means that the characteristic time scale for the density to grow is about 24 IAW periods, in this case. The saturation level $\delta n_{\text{sat}} = 8.7 \times 10^{-5}$, obtained at time $t = 1.4 \times 10^5\ \omega_{pe}^{-1}$, is of the order of the expected saturation level defined by the ratio of electric energy to the thermal energy $\delta n_{\text{sat}}^0 = \frac{1}{2} E_L^2/(T_e + T_i) = 2.3 \times 10^{-4}$. The simulation has been repeated for several initial Langmuir wave amplitude, with values in the range $10^{-3} < E_L < 1$, and for two temperature ratios $\Theta = 0.1$ and $\Theta = 1$.

[22] We found that the evolution becomes strongly nonlinear when the Langmuir wave electric field is "not small," i.e., when $E_L \gtrsim 0.3$ for $\Theta = 1$ and $E_L \gtrsim 0.2$ for $\Theta = 0.1$. When strong non linear processes take place the evolution is

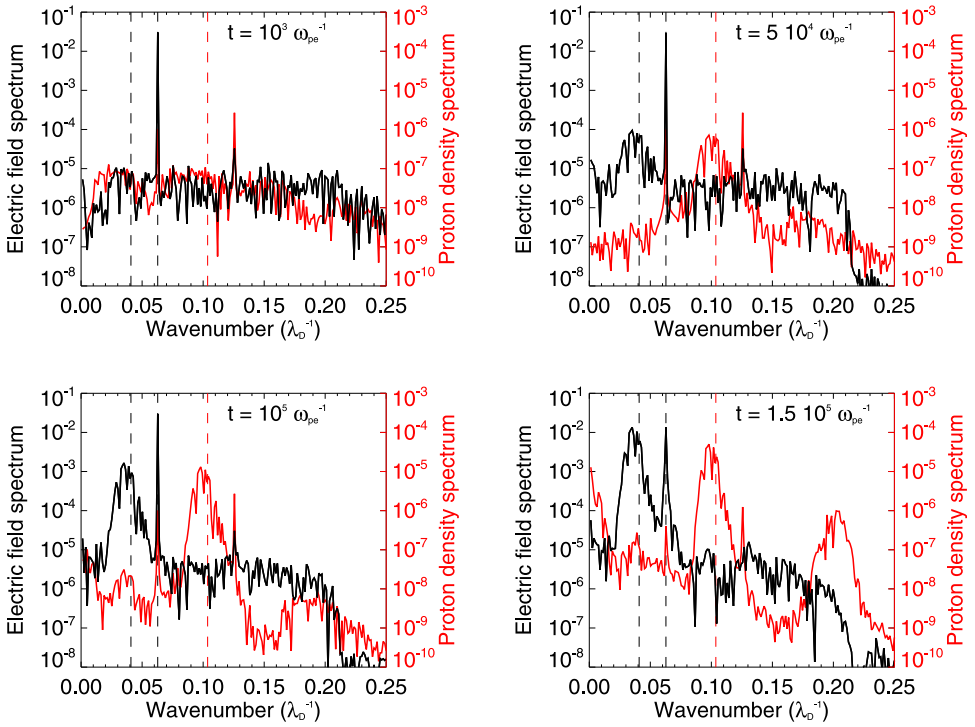

Figure 1. Spectrum of both electric field (in black) and ion density (in red) at four different times from simulation of LED of a monochromatic Langmuir wave with wave number $k_L = 0.063$ and initial electric amplitude $E_L = 3 \times 10^{-2}$. Dashed lines indicate the expected wave numbers of the LED waves. (top left) Initial conditions. (bottom right) Spectrum at saturation. Note the presence of the second harmonic of the IAW in this last case.

not simply driven by the LED mechanism. Conversely, for small values of E_L, the system is mainly driven by the LED process so that we can compute the growth rate for average density fluctuations and the density fluctuations saturation level as previously defined.

[23] The growth rate deduced from simulations γ_{LED} of the average density fluctuations $\langle \delta n \rangle$ deduced from the simulation is displayed in Figure 3 for the two temperature ratios. As shown before, for too high values of the Langmuir amplitude, about $E_L \simeq 0.3$, corresponding to an electric to thermal energy ratio of 0.1, strong nonlinear effects arise before LED. Also, as expected, the growth rates are lower for $\Theta = 1$ than $\Theta = 0.1$, due to the increase of IAW Landau damping in the first case. Contrary to former results [*Umeda and Ito*, 2008], we show here that the LED is observed for initial Langmuir waves with electric energy 5 orders of magnitude lower than the plasma thermal energy.

[24] An analytical effective growth rate $\gamma_{\mathrm{LED}}^{\mathrm{analytical}}$ has been overplotted (dashed lines). It is defined as the difference between the analytical full monochromatic case of undamped monochromatic waves in an homogeneous background $\gamma_{\mathrm{LED}}^{\mathrm{th}}$ [*Sagdeev and Galeev*, 1969] and the IAW Landau damping $\gamma_S^{\mathrm{Landau}}$:

$$\gamma_{\mathrm{LED}}^{\mathrm{analytical}} = \gamma_{\mathrm{LED}}^{\mathrm{th}} - \gamma_S^{\mathrm{Landau}}, \tag{9}$$

where

$$\gamma_{\mathrm{LED}}^{\mathrm{th}} \simeq k_{IA} C_s \left(\frac{\epsilon_0 E^2}{n k_B T} \frac{m_p}{m_e} \right)^{1/4}; \tag{10}$$

$\gamma_{\mathrm{LED}}^{\mathrm{th}}$ is of the order of the IAW frequency with solar wind parameters. The growth rate computed from Vlasov simulations γ_{LED} is 1–2 orders of magnitude lower than $\gamma_{\mathrm{LED}}^{\mathrm{analytical}}$. The discussion concerning the discrepancy

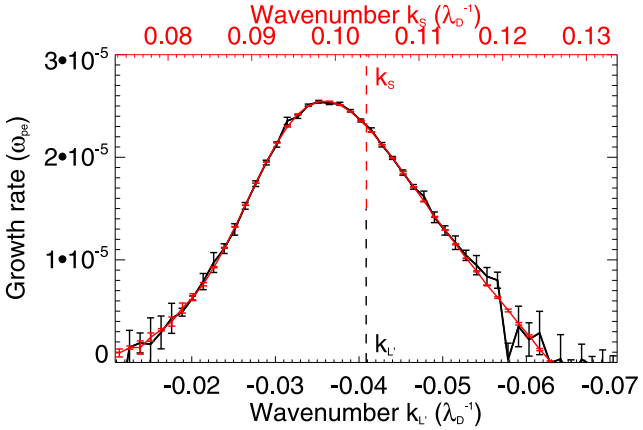

Figure 2. Spectral growth rate for the Langmuir wave L' electric field (in red, $k_{L'}$ axis at the bottom, leftward) and the IAW density fluctuations (in black, k_S-axis at the top, rightward) generated by the LED of a monochromatic Langmuir wave ($E_L = 3 \times 10^{-2}$ and $\Theta = 1$). Both axes are scaled to show the resonant condition in wave numbers: $k_S + k_{L'} = k_L$. Vertical error bars are $1 - \sigma$ error bars for the fitting of the growth rate. The vertical dotted line indicates the expected wave numbers for monochromatic LED products.

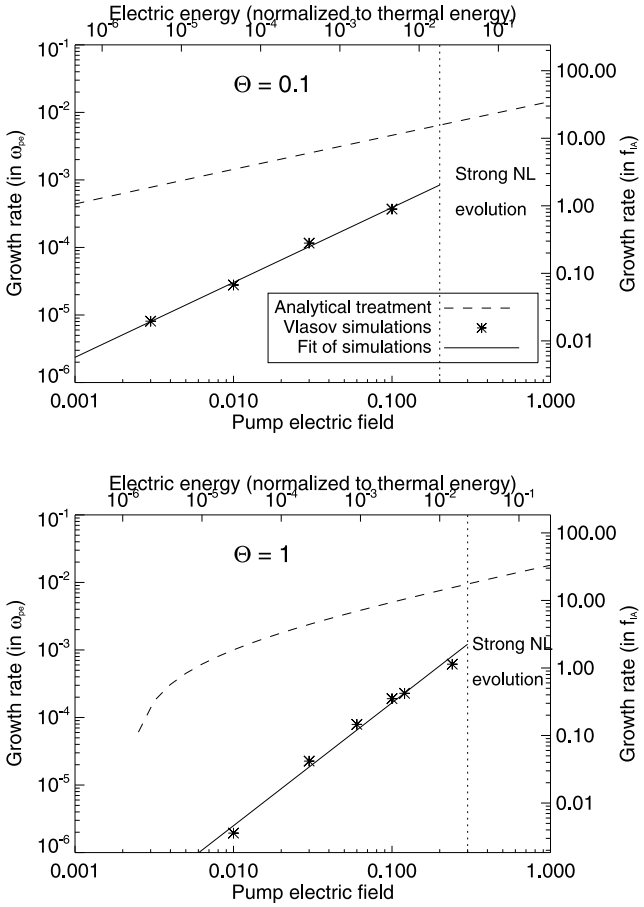

Figure 3. Growth rate for IAW density fluctuations versus Langmuir wave initial electric field amplitude for two temperature ratios. (top) $\Theta = 0.1$. (bottom) $\Theta = 1$. The growth rate is expressed in (left) plasma frequency unit ω_{pe} and in (right) IAW frequency f_{IA}. The full line is a fit of Vlasov simulations (stars). The dashed line shows the analytical growth rate $\gamma_{\mathrm{LED}}^{\mathrm{analytical}}$ from *Sagdeev and Galeev* [1969] when LED-generated IAW remain monochromatic, including the linear Landau damping of IAW. The vertical dotted line sets the limits above which strong nonlinear effects occur before LED starts.

between the analytical monochromatic case and Vlasov simulations is postponed to section 4.2.

[25] We also looked for the dependence of the growth rate with respect to the mother Langmuir wave vector k_L. Finally, the growth rate for density fluctuations generated by LED has been fitted by a power law:

$$\gamma_{\mathrm{LED}} = \Gamma\, E_L^{\alpha} k_L^{\beta}. \tag{11}$$

The fitting parameters Γ, α and β are given in Table 2.

[26] The saturation level of density fluctuation δn_{sat} is summarized in Figure 4 for $\Theta = 0.1$ (Figure 4, top) and $\Theta = 1$ (Figure 4, bottom). The expected saturation level $\langle \delta n_0^{\mathrm{sat}} \rangle$, expressed as the initial Langmuir electric energy to the total kinetic energy ratio,

$$\langle \delta n_0^{\mathrm{sat}} \rangle = \frac{1}{2} E_L^2/(T_e + T_i), \tag{12}$$

is overplotted (dashed lines). The obtained saturation level of density fluctuation is in good agreement with the expected values in both cases.

[27] To summarize, the simulations of the Langmuir electrostatic decay from an initial monochromatic Langmuir wave have shown that (1) the threshold for the instability to grow, expressed in term of the Langmuir wave electric energy, is at least 5 orders of magnitude lower than the plasma thermal energy when $0.1 < \Theta < 1$; (2) the product waves are resonantly generated over a broad range of wave numbers, naturally producing narrow wave packets; (3) growth rates of IAW density fluctuations are 1–2 orders of magnitude lower than the analytical values deduced from the pure monochromatic case; and (4) saturation levels for IAW relative density fluctuations are of the order of the ratio of Langmuir electric energy to the total kinetic energy.

3.2. Electrostatic Decay of a Langmuir Wave Packet

[28] In the following, we consider the evolution of a finite-amplitude Langmuir wave packet, generated by the external electric field pump defined in equation (B2). We recall that, in order to mimic the presence of a low level of small-scale ion acoustic turbulence, we introduce a source term of ion acoustic noise. This forcing generates incoherent proton density fluctuations at a level $\delta n/n \sim 10^{-5}$ much smaller than the expected level of density fluctuations generated by LED.

[29] Figure 5 shows the LED of a Langmuir wave packet with wavelengths centered on $\lambda_L = 200\ \lambda_D$, a packet width $\Delta = 2000\ \lambda_D$, a maximum initial electric field $E_L = 6 \times 10^{-2}$, and the two temperature ratio $\Theta = 0.1$ (Figure 5, left) and $\Theta = 1$ (Figure 5, right). The mother and daughter Langmuir wave packets can be followed in Figure 5 (top) that show the space-time evolution of the electric field density energy $E(x, t)^2/2$. The Langmuir mother wave packet propagates toward the right and emits backscattered Langmuir wave packets. Figure 5 (bottom) shows the temporal evolution of ion density fluctuations during the decay of the Langmuir wave. IAW density fluctuations are generated locally (by ponderomotive force from the two Langmuir wave packets beats) and propagate forward at the ion sound speed (dashed line). When $\Theta = 0.1$ IAW propagate and escape the area where LED develops. Conversely, when $\Theta = 1$, IAW density fluctuations are heavily damped as soon as the waves escape the area where LED occurs. Thereby, the waves can be observed only where the mother Langmuir wave decays. Finally, as for the case of monochromatic Langmuir waves, the LED growth rate is lower for a larger value of Θ.

[30] The simulation has been repeated for different values of E_L and mean wavelength λ_L, with a packet width of $\Delta = 10\ \lambda_L$. Figure 6 summarizes the results for the evolution of the Langmuir wave packet, each point representing a single simulation.

Table 2. Numerical Values for the Fit for the Growth Rate of LED-Driven Density Fluctuations in Equation (11)

	Γ	α	β
$T_p/T_e = 0.1$	0.026	1.11	0.59
$T_p/T_e = 1$	0.025	1.82	0.30

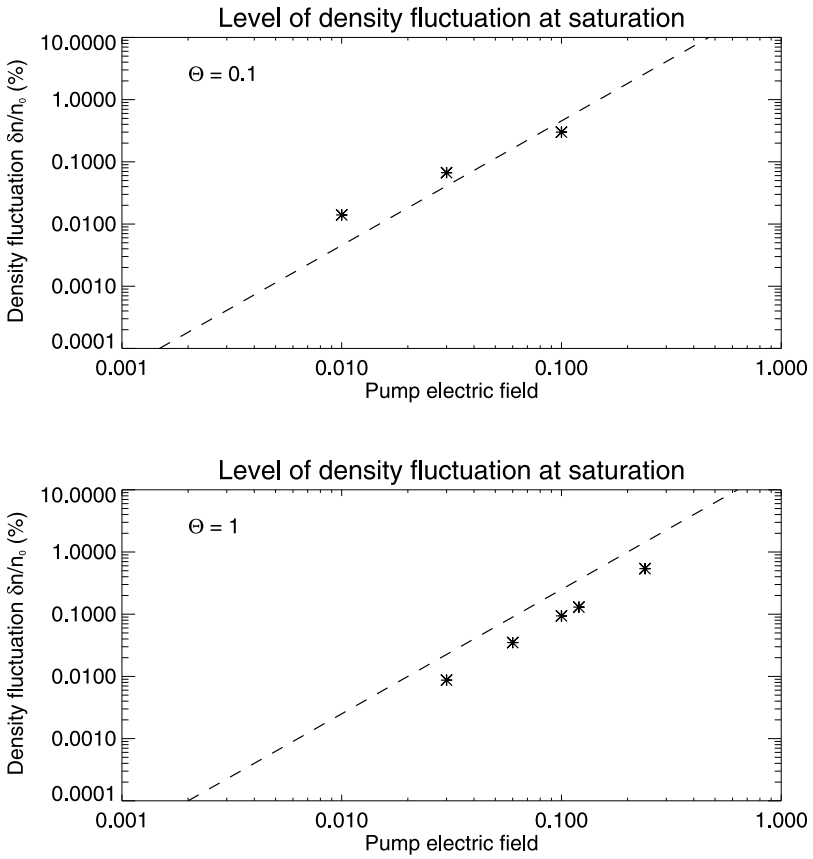

Figure 4. Average density fluctuation at saturation δn_{sat} (expressed in percentage of mean density) for different Langmuir wave initial electric field amplitudes for both (top) $\Theta = 0.1$ and (bottom) $\Theta = 1$. The dashed lines show the expected level of saturation $\delta n_0^{\mathrm{sat}} = (0.5 \times E_L^2)/(T_e + T_i)$ defined as the Langmuir electric energy to the total kinetic energy ratio.

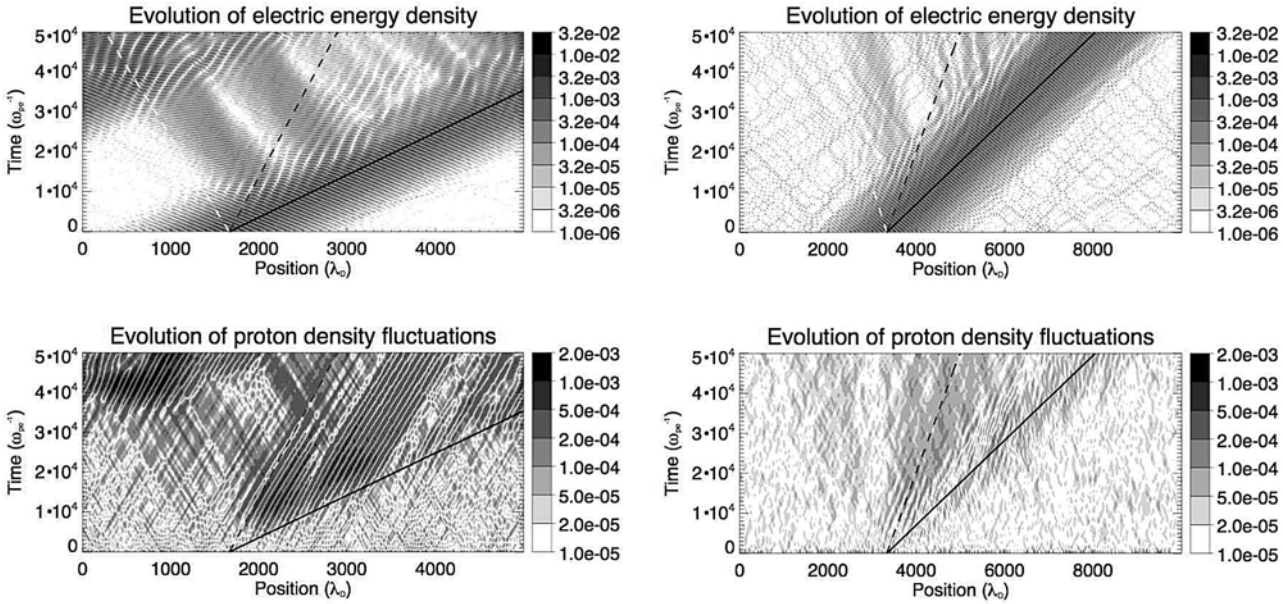

Figure 5. (top) Space-time evolution of the electric energy density. (bottom) Space-time evolution of the ion density fluctuations. (left) $\Theta = 0.1$. (right) $\Theta = 1$. Full lines show the expected group velocities of the Langmuir wave packets, while dashed lines display the ion sound speed.

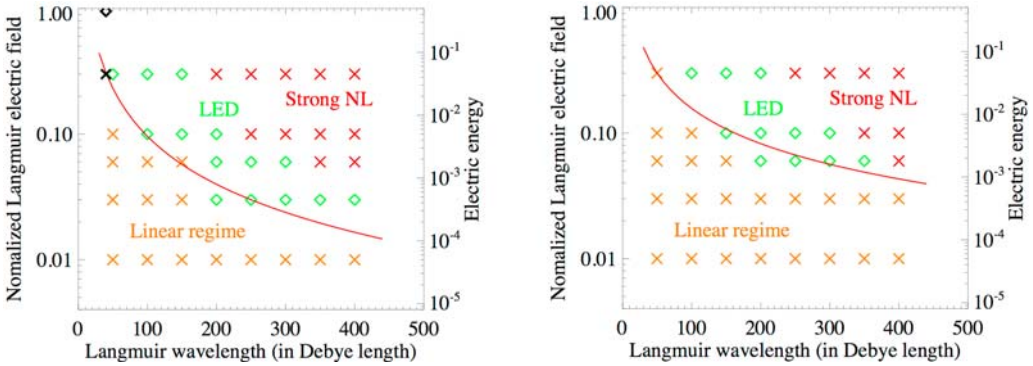

Figure 6. Evolution of a Langmuir wave packet, (bottom) with different wavelengths centered on λ_L but a same packet width of $\Delta = 10\ \lambda_L$ and different initial electric fields E_L (left axis). (left) $\Theta = 0.1$. (right) $\Theta = 1$. In green are simulations where LED is observed; in orange are simulations where the available interaction time between the waves is lower than the LED time scale; in red are simulations where strong NL effects arise before/instead of LED. Previous simulation results from *Umeda* [2007] and *Umeda and Ito* [2008] are overplotted in Figure 6 (left) with black crosses and diamonds, respectively. The red line is the semianalytical threshold expressed in equation (15).

[31] During the decay process, the mother wave packet generates a daughter wave packet traveling at a different group velocity. The region of parameters leading to electrostatic decay is displayed with green squares in Figure 6. Eventually the two wave packets separate thus stopping the LED process. Therefore, LED is efficient only if the interaction time between the two wave packets is longer than the growth time for the daughter waves. The growth time of the instability is controlled by the Langmuir electric field amplitude: the larger the amplitude, the smaller the growth time (Figure 3). The interaction time is controlled by the Langmuir wavelength: the larger the wavelength, the smaller its group velocity and so the larger the interaction time. Thus, for low-amplitude and/or short wavelengths, the Langmuir wave packet propagates at its group velocity without nonlinear interactions. The region of parameters leading to a linear behavior without electrostatic decay is displayed with orange crosses in Figure 6. The efficiency of LED (green) region increases toward the linear (orange) part (i.e., LED is observed for lower λ_L and E_L) if temperature ratio Θ decreases or/and the size Δ of the mother wave packet increases. Finally, strong non linear effects dominate the evolution of high-amplitude and/or large-wavelength Langmuir wave packets, and LED is no more the dominant process. The region of parameters where other non linear effects are dominant is shown with red crosses in Figure 6. These strong non linear effects seem to be the signature of strong turbulence: Langmuir collapse and formation of cavitons. This evolution is out of scope of the present study and will be studied in a future work.

[32] The effective threshold for the electrostatic decay of a Langmuir wave packet can be estimated by imposing that the interaction time τ_{int} is equal to the inverse growth rate of daughter wave packets γ_{LED}. The growth rate for LED γ_{LED} has been obtained from simulations of monochromatic Langmuir waves LED and fitted in equation (11). The interaction time τ_{int} is evaluated from

$$\tau_{int} \simeq \Delta/(v_L^g - v_{L'}^g), \tag{13}$$

where $(v_L^g - v_{L'}^g)$ is the difference of group velocity between the two waves that first separate, here the mother and daughter Langmuir waves, and Δ the packet width of the mother Langmuir wave, which is assumed to be about the length of interaction. Using equation (1) and $k_S \simeq 2\ k_L$, equation (13) can be written in normalized units as

$$\tau_{int} \simeq \Delta/(6\ k_L). \tag{14}$$

Finally, $\tau_{int} = \gamma_{\mathrm{LED}}^{-1}$ gives the effective LED threshold of a Langmuir wave packet with wave vector k_L and a packet width Δ:

$$E_{\mathrm{LED}}^{\mathrm{threshold}} = \left(\frac{6\ k_L^{1-\beta}}{\Delta\Gamma}\right)^{1/\alpha}, \tag{15}$$

expressed in normalized units. The semianalytical threshold is overplotted in Figure 6 (red line) in order to validate its dependency with the mother Langmuir wave vector k_L.

[33] We also performed a series of simulations in order to validate the dependency of $E_{\mathrm{LED}}^{\mathrm{threshold}}$ with Δ. This time the simulation starts with a mother Langmuir wave packet of mean wavelength $\lambda_L = 200$ but with different packet width values in the range $5\ \lambda_L < \Delta < 30\ \lambda_L$, covering the typical range for Langmuir wave packets in the solar wind, and initial amplitude E_L. The results are presented in Figure 7, together with the semianalytical threshold (red line). In both cases, equation (15) is in agreement with simulations of LED of localized Langmuir wave packets.

[34] The threshold decreases when (1) the ion to electron temperature ratio decreases, since the Landau damping of IAW decreases and their effective growth rate increase; (2) the mean Langmuir wavelength increases, since Langmuir wave packets with longer wavelengths propagate at smaller group velocities thus increasing the available interaction time with the ion background; and (3) the width of the Langmuir wave packets increases, since the interaction time between the mother and daughter waves increases. The effective threshold obtained by Vlasov simulations and described in this section is compared to observations of LED in the solar wind in the next section.

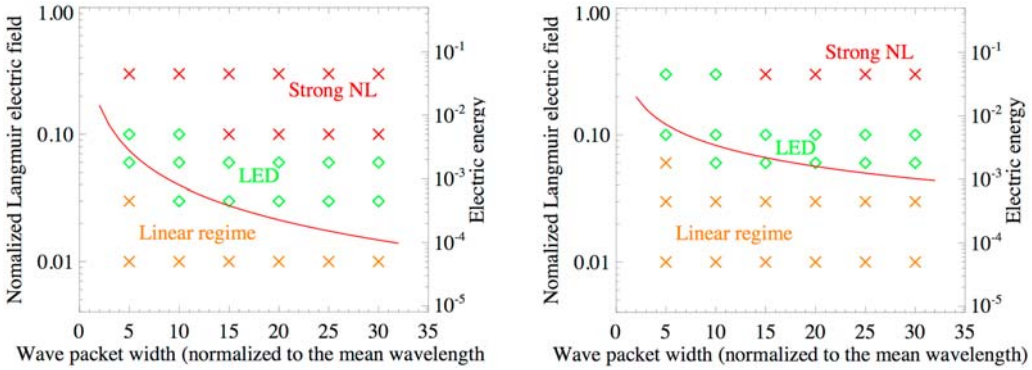

Figure 7. Evolution of a Langmuir wave packet with a mean wavelength $\lambda_L = 200$ but different packet widths Δ (bottom axis, normalized to λ_L) and different initial electric fields E_L (left axis). (left) $\Theta = 0.1$. (right) $\Theta = 1$. In green are simulations where LED is observed; in orange are simulations where the available interaction time between the waves is lower than the LED time scale; in red are simulations where strong NL effects arise before/instead of LED. The red line is the semianalytical threshold expressed in equation (15).

[35] Finally, in two recent works of 1D-1V Vlasov simulations, *Umeda* [2007] and *Umeda and Ito* [2008] reported the evolution of beam-excited Langmuir waves. Their simulation parameters are $\Theta = 0.1$, a beam speed $v_{beam} = 8 \times v_{th,e}$ with a beam temperature equals to the electron core temperature and a beam density ratio of 0.1% and 0.5%, respectively. These beams generate Langmuir waves at a phase velocity of about $v_{beam} - v_{th,e} = 7 \times v_{th,e}$, i.e., a Langmuir wavelength $\lambda_L \simeq 40 \times \lambda_D$. The amplitude of the Langmuir waves reaches $E_L \sim 0.3$ in the first case, $E_L \sim 1$ in the second case. They observed the LED process in the second case only. We have overplotted their results in Figure 6 (black cross and diamond, respectively). These previous simulations agrees with equation (15): for these parameters, the equation predicts that LED of localized Langmuir wave packets should occur for high Langmuir electric energy levels (of the order of unity).

[36] To summarize the simulations of the Langmuir electrostatic decay from an initial Langmuir wave packet: (1) we have illustrated how the localization of Langmuir wave packets is crucial for the evolution of Langmuir decay by limiting the interaction time between mother and daughter waves; (2) we have shown that the ion acoustic waves are generated locally, where the wave packets interact, and then IAW are damped as soon as they escape the region where the mother and daughter Langmuir waves interact when electron and ion temperature are equal or escape this region when the electron temperature is higher than the ion temperature; and (3) we used results from the Langmuir electrostatic decay of a monochromatic Langmuir wave (section 3.1) to compute a semianalytical threshold for the electrostatic decay of Langmuir wave packets (equation (15)); this semianalytical threshold has been shown to be in agreement with simulations of the electrostatic decay of Langmuir wave packets.

4. Discussion

[37] In the following, we discuss, first, the initialization of LED in the case $\Theta = 1$, second, the discrepancy between the LED growth rate obtained from simulations and analytical estimation. LED threshold obtained from simulations is then compared to observations. Finally, we show that the saturation of the instability gives an upper limit to the expected level of observed density fluctuations.

4.1. Initialization of Langmuir Electrostatic Decay

[38] In the case of equal electron and ion temperature, associated with a strong Landau damping of ion acoustic fluctuations, one may wonder whether processes complementary to the resonant interaction of the waves could facilitate the LED. In particular, a decrease (even local) of the IAW Landau damping during the beginning of the LED process could ease the initialization of the instability. Such decrease can happen either through two main processes. (1) Wave-particle interactions due to the trapping of ions in the IAW potential well could modify the ion distribution function by forming a plateau at the ion sound speed which, in turn, could then decrease the Landau damping rate. However, no such plateauing is observed. (2) The beats of the mother and daughter Langmuir waves, could heat the electrons so that the ion-to-electron temperature ratio decrease locally, leading to a partial suppression of the IAW Landau damping. However the temperature ratio during the simulation has too small variations $\Delta\Theta/\Theta < 1\%$ to really modify the IAW Landau damping. This hypothesis is thus also ruled out.

[39] Since no such complementary processes are present in the simulations, the initiation of the LED is likely to be caused by the resonant interaction of the waves, that dominates locally the Landau damping of IAW.

4.2. Growth Rate for Langmuir Electrostatic Decay

[40] We have seen in section 3.1 that a large discrepancy exists between the growth rate of mean density fluctuations obtained from the simulations, γ_{LED}, and the analytical one deduced from three monochromatic waves, γ^{th}_{LED} [*Sagdeev and Galeev*, 1969]. (The influence of the resolution in velocity has been checked, and the results are unchanged as far as the resolution in velocity is not too low. The results

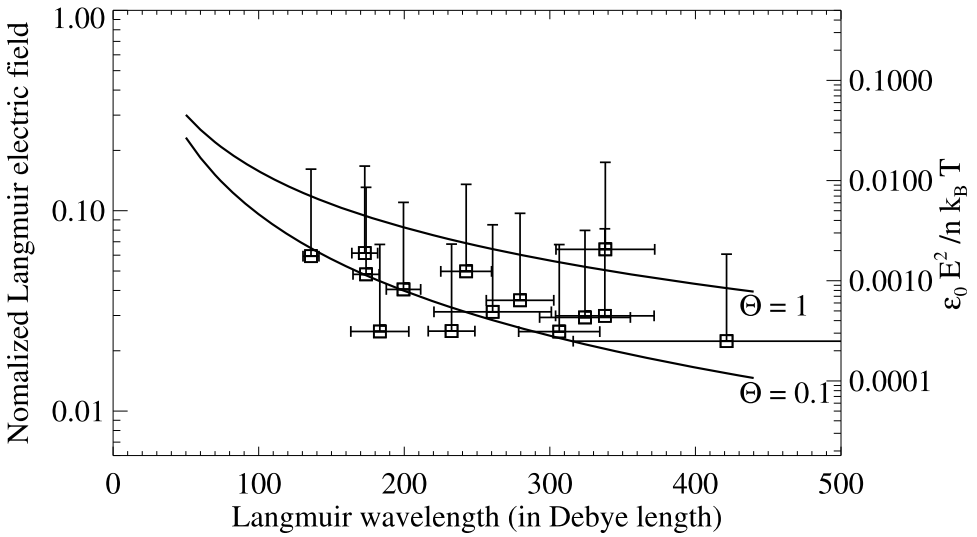

Figure 8. Observed Langmuir electric field amplitude, normalized like the simulations, versus wavelength. The threshold for LED computed from Vlasov simulations is overplotted for two values of the temperature ratio $\Theta = 0.1$ and $\Theta = 1$.

are also independent of the size of the box, as long as the box remains larger than the coherence length of the daughter wave packets.) The existence of a strong IAW Landau damping γ_{Landau}, such that $\gamma_{\text{LED}} = \gamma_{\text{LED}}^{\text{th}} - \gamma_{\text{Landau}}$ could explain this difference. Since Landau damping for IAW cannot be found analytically when electron and temperature are close, we performed complementary simulations and measured an IAW Landau damping of $\gamma_{\text{Landau}} = -1.9 \times 10^{-5}\ \omega_{pe}$ for $\Theta = 0.1$ ($\gamma_{\text{Landau}} = -8.9 \times 10^{-4}\ \omega_{pe}$, respectively, for $\Theta = 1$), much lower than γ_{th}. Thus, the hypothesis that $\gamma_{\text{LED}} = \gamma_{\text{LED}}^{\text{th}} - \gamma_{\text{Landau}}$ is to be ruled out.

[41] Note that the growth rate measured from simulations already takes into account the effect of the Landau damping. Thus, the difference between γ_{LED} and $\gamma_{\text{LED}}^{\text{analytical}}$ should be carried by the evaluation of $\gamma_{\text{LED}}^{\text{th}}$. Actually, the main difference between the analytical treatment of three-wave resonance and Vlasov simulations is that the daughter waves are treated as monochromatic in the first case whereas they are observed to have a non negligible spectral width in the second (see Figures 1 and 2). Simulations have shown that the spectral width of the product waves increases when (1) $\Theta \simeq 1$, in which case the IAW dispersion relation is numerically observed to spread out around the analytical branch; therefore the resonance can occur with (ω, k) values slightly different from the theoretical expectation; and (2) the energy of the Langmuir mother wave increases, in which case the linear approximation for a δ-shaped resonance is no longer valid. The limited spatial coherence of daughter wave packets implies that their growth is localized where mother and daughter wave packets interact, thus strongly limiting their growth rate. This explains why the growth rate deduced from simulations is much lower than the analytical one.

4.3. Threshold of Langmuir Electrostatic Decay and Type III Observations

[42] The TDS observation mode of the S/WAVES experiment on board the STEREO mission [*Bougeret et al.*, 2007] gives access to in situ electric field waveform in 3D with an equivalent spectral resolution up to 60 kHz. In Paper I, we have shown evidence for nonlinear coupling between Langmuir waves at about 10 kHz and ion acoustic waves at about 0.2 kHz. We recall here the global plasma parameters for these observations. The 1-h-average wind speed from WIND/3-DP [*Lin et al.*, 1995] is about $V_{SW} = 315$ km s^{-1}. The electron temperature observed by WIND/3DP is $T_e \simeq 10^5$ *K*, and the electron density in the solar wind, estimated from the plasma frequency, is about $n_e \simeq 10^6$ m^{-3}. From the electron density and temperature, the Debye length is $\lambda_D \simeq 20$ m.

[43] Figure 8 displays the observed value of Langmuir electric field, normalized as described in equation (7), for the whole data set of waveforms where LED has been observed. Their wavelength, not directly measured, is evaluated as follows. By taking into account the Doppler shift caused by the solar wind and noting that the IAW should propagate here antisunward, the ion acoustic wavelength reads:

$$\lambda_S = (V_{SW} + c_s)/f_S^{\text{obs}}$$

where the sound speed c_s is evaluated by

$$c_s = \sqrt{k_B(T_e + T_p)/m_p},$$

where k_B is the Boltzman constant, m_p the proton mass and T_p the proton temperature that remains unknown but is of the order of T_e in the solar wind. The mother Langmuir wavelength λ_L is then about twice the LED-produced ion acoustic wavelength.

[44] However, caution should be taken when directly comparing this threshold value with the observation. Indeed solar wind type III Langmuir wave packets are most probably localized in 3D. The observed waveforms are 1D spatial cuts of the real 3D structures and thus only give a lower limit on the width of the wave packet, as well as its

maximum amplitude. We assume that the Langmuir wave packets have a 3D gaussian shape, and that the spacecraft crosses it somewhere within a distance from the center of the 3D structure of the order of the full width at half maximum. Therefore a realistic range for the maximum electric field E_L^{real} reached by the 3D wave packet is calculated as: $E_L^{\text{obs}} \lessapprox E_L^{\text{real}} \lessapprox e\, E_L^{\text{obs}}$, where E_L^{obs} is the observed level of Langmuir electric field. Data are plotted with such error bars.

[45] The LED threshold expressed in equation (15) is overplotted for two values of the ion to electron temperature ratio $\Theta = 0.1$ and $\Theta = 1$, using computed values from Table 2. The observed electric field amplitudes are of the order of the threshold computed from Vlasov-Poisson simulations, in the case of a localized wave packet and $\Theta \approx 1$, confirming that the development of LED is compatible with the observed events.

4.4. Saturation of LED: Expected Level of Observed Density Fluctuations

[46] In our simulations, for initial Langmuir wave packets in the range of amplitudes that correspond to observations of Langmuir waves during type III events, the IAW-like density fluctuations associated with the LED do not reach the saturation level. Indeed, the mother and Langmuir wave packets that propagate at different group velocities separate before the saturation stage, thus stopping the growth of the IAW. This is confirmed in the observations, since most of the observed waveforms show (1) mother and daughter Langmuir waves with different energies and (2) IAW with no harmonics. The saturation level $\langle \delta n_0^{\text{sat}} \rangle / n_0 = E_L^2/(T_e + T_i)$ should thus be an upper limit on the expected level of density fluctuations on observations of LED during type III.

[47] Density fluctuations at the frequencies considered here can be measured in space from the variations of the floating potential of the spacecraft [*Pedersen*, 1995] when it crosses the region where LED is observed. The voltage signal observed on STEREO/Waves waveforms with monopole antennas channels contains information on the floating potential of the spacecraft. This remains however to be calibrated. Knowing the saturation level of IAW during LED, and given the calibration, we could check whether the observed level of density fluctuations is consistent with our simulations.

5. Conclusion

[48] In order to study the origin of electromagnetic radio emissions during type III bursts, we have reported in this paper 1D-1V Vlasov-Poisson simulations of the Langmuir electrostatic decay. The simulations have been done in typical solar wind conditions: ratio of the electron to ion temperature from 0.1 to 1, mother Langmuir wavelengths typical of those observed during type III events and, most important, by considering localized Langmuir wave packets. The main results are the following.

[49] 1. Langmuir electrostatic decay develops even when the electron and ion temperatures are close. Its threshold, when considering a monochromatic wave, is at least 5 orders of magnitude lower than the plasma thermal energy when $0.1 < \Theta < 1$.

[50] 2. Langmuir electrostatic decay resonantly generates daughter waves over a broad range of wave numbers, naturally leading to narrow wave packets. This limits the length of coherence which is why the growth rate is 1–2 orders of magnitude lower than the analytical values deduced from a pure monochromatic case.

[51] 3. The behavior of daughter ion acoustic waves depends on the temperature ratio. Ion acoustic waves can escape the region where the resonant coupling takes place and propagate when electron temperature is higher than proton temperature. Conversely, they are damped as soon as they escape the resonant coupling area when temperatures are equal.

[52] 4. We confirm that the saturation level for IAW density fluctuations is of the order of the ratio of Langmuir electric energy to the total kinetic energy. However, for the range of amplitudes that correspond to observations, the IAW-like density fluctuations associated with the LED should not reach the saturation level because (1) the mother and Langmuir wave packets that propagate at different group velocities separate before the saturation stage and (2) harmonics of the IAW are seen at saturation in the simulations but, to our knowledge, not in type III observations.

[53] 5. Finally, an effective threshold has been obtained (equation (15)) for localized Langmuir wave packets and compared to STEREO/WAVES observations. The observed Langmuir electric field during type III reported by *Henri et al.* [2009] is in the range of LED effective threshold computed from Vlasov simulations, thus confirming the interpretation of these observed electric field waveforms in term of the LED of type III beam-driven Langmuir waves.

[54] The physical mechanism responsible for the generation of electromagnetic radio waves during type III burst is still under study. The process described by *Ginzburg and Zheleznyakov* [1958] and leading to the generation of type III radio emission at twice the local plasma frequency is a two step process: (1) first the beam-driven Langmuir wave decays through LED, then (2) the mother and daughter Langmuir waves coalesce to generated the electromagnetic wave.

[55] Up to now, observations have shown that resonant coupling between Langmuir waves and ion acoustic waves does occur during a type III burst [*Henri et al.*, 2009]. The present paper also shows that Langmuir electrostatic decay may occur in solar wind conditions and that the threshold is reached by the observed Langmuir electric amplitude. These two complementary studies thus confirms step 1 does occur.

[56] Langmuir electrostatic decay generates two counterpropagating Langmuir waves in opposite direction, but step 2 requires obliquely propagating Langmuir waves for waves to couple and produce the transverse electromagnetic wave. Does the density inhomogeneities scatter the Langmuir waves enough to introduce a significant perpendicular component to their wave vector? An important step would be to study the interaction of Langmuir waves with an inhomogeneous background, in order to check this hypothesis. Finally, the coalescence of counterpropagating Langmuir waves is hard to observe because the signal would be hidden by the generation of the harmonic of the mother Langmuir wave. Simulations of step 2 with input from the observations

could at least show whether the coalescence process could occur in the solar wind.

Appendix A: Generation of the Ion Density Noise

[57] The continuous injection of ion density noise is driven by an external fields $E_{\rm ext}^{\rm noise}$ added to the ion dynamics (equation (3)). This driver is defined by

$$E_{\rm ext}^{\rm noise}(x,t) = E_{\rm ext}^{\rm ions,max} \frac{\sum_\lambda \cos(2\pi x/\lambda)\cos(\omega_\lambda t + \Psi''_\lambda(t))}{|\sum_\lambda \cos(2\pi x/\lambda)\cos(\omega_\lambda t + \Psi''_\lambda(t))|}. \quad \text{(A1)}$$

It introduces a flat spectrum for wavelength over the range $50 < \lambda < 1000$. $E_{\rm ext}^{\rm noise}(x, t)$ is normalized in order to have a maximum amplitude of $E_{\rm ext}^{\rm ions,\ max} = 1 \times 10^{-5}$. The frequencies ω_λ are chosen to satisfy the dispersion relation of IAW, $\omega_\lambda = (2\pi/\lambda)c_s$ with $c_s = \sqrt{(1+\Theta)/\mu}$ the ion sound speed. The phases $\psi''_k(t)$ have a steplike variation, constant over a time interval δt. At the end of each interval, they are independently drawn from a uniform distribution. This way, the generation of ion acoustic noise is made of a succession of time coherent forcing for time intervals of duration $\delta t = 500 \times \omega_{pe}^{-1}$ (about 80 plasma oscillations). This means that for an IAW of wavelength $\lambda_{IA} = 100$, the forcing lasts 1/20th of a period, much shorter than the typical IAW oscillation time in order to generate an incoherent noise. This forcing thus generates density fluctuations much smaller than the level of density fluctuations generated by LED in our simulations.

Appendix B: Generation of the Initial Langmuir Wave

[58] In this appendix, we describe the driver $E_{\rm ext}^{\rm init}$, added in the Vlasov equation for electrons (equation (2)). This external electric field controls the generation of the initial Langmuir wave. It acts as a driver that resonantly grow a Langmuir wave propagating in only one direction, with the desired spectrum and electric field amplitude. In section 3.1, a monochromatic Langmuir wave of wavelength λ_L and amplitude E_L is resonantly excited by the external electric field pump by defining $E_{\rm ext}^{\rm init} = E_{\rm ext}^{(1)}$:

$$E_{\rm ext}^{(1)}(x,t) = E_0^{(1)}(t)\ \cos(k_0 x - \omega_0 t). \quad \text{(B1)}$$

In section 3.2, a Langmuir wave packet of mean wavelength λ_L, packet width Δ and maximum amplitude E_L is resonantly excited by defining $E_{\rm ext}^{\rm init} = E_{\rm ext}^{(2)}$.

$$E_{\rm ext}^{(2)}(x,t) = E_0(t)\ \cos(k_0 x - \omega_0 t)\ \exp\left(-\left(\frac{x - x_0 - v_L^g t}{0.5\Delta}\right)^2\right). \quad \text{(B2)}$$

In both cases, the pump wave vector $k_0 = 2\pi/\lambda_L$ and the frequency $\omega_0 = \sqrt{1 + 3k_0^2}$ are chosen to satisfy the Langmuir dispersion relation, in order to generate a Langmuir wave at the desired wavelength λ_L. The width of the wave packet is set to $\Delta = 10\ \lambda_L$. The pump wave packet moves at the Langmuir group velocity $v_L^g = 3k_0/\omega_0$ from its initial position $x_0 = L_x/3$. The time-dependant external electric field amplitude $E_0(t)$ scales on the desired Langmuir amplitude E_L:

$$E_0^{(1)}(t) = \eta E_L(1 - \exp(-t/\tau)). \quad \text{(B3)}$$

In the monochromatic case (wave packet case, respectively), the parameter τ is set to 30 ω_{pe}^{-1} (100 ω_{pe}^{-1}, respectively) so that the external electric field amplitude smoothly increases during a few Langmuir oscillations, in order to avoid the generation of other plasma waves induced by steplike switch of the pump. The parameter η is set experimentally to 5×10^{-2} (10^{-2}, respectively), so that the characteristic time scale to resonantly grow the Langmuir wave (wave packet, respectively) is large compared to its oscillation time scale, but small compared to the decay time scale. So, the resonant generation of the Langmuir wave (wave packet, respectively) does not interfere with the LED mechanism.

[59] **Acknowledgments.** We are grateful to the Italian supercomputing center CINECA (Bologna), where part of the calculations were performed. We also acknowledge C. Cavazzoni for discussion on code performance.

[60] Philippa Browning thanks Takayuki Umeda and another reviewer for their assistance in evaluating this manuscript.

References

Akimoto, K., Y. Omura, and H. Matsumoto (1996), Rapid generation of Langmuir wave packets during electron beam-plasma instabilities, *Phys. Plasmas*, *3*, 2559.

Bale, S. D., D. Burgess, P. J. Kellogg, K. Goetz, R. L. Howard, and S. J. Monson (1996), Phase coupling in Langmuir wave packets: Possible evidence of three-wave interactions in the upstream solar wind, *Geophys. Res. Lett.*, *23*, 109.

Bardwell, S., and M. V. Goldman (1976), Three-dimensional Langmuir wave instabilities in type III solar radio bursts, *Astrophys. J.*, *209*, 912.

Bougeret, J. L., et al. (2007), S/WAVES: The Radio and Plasma Wave Investigation on the STEREO Mission, *Space Sci. Rev.*, *136*, 487.

Cairns, I. H., and P. A. Robinson (1992), Theory for low-frequency modulated Langmuir wave packets, *Geophys. Res. Lett.*, *19*, 2187.

Cairns, I. H., and P. A. Robinson (1995), Ion acoustic wave frequencies and onset times during type III solar radio bursts, *Astrophys. J.*, *453*, 959.

Celnikier, L. M., L. Muschietti, and M. V. Goldman (1987), Aspects of interplanetary plasma turbulence, *Astron. Astrophys.*, *181*, 138.

Dulk, G. A., M. V. Goldman, J. L. Steinberg, and S. Hoang (1987), The speeds of electrons that excite solar radio bursts of type III, *Astron. Astrophys.*, *173*, 366.

Dysthe, K. B., and R. N. Franklin (1970), Non-linear interactions of coherent electrostatic plasma waves, *Plasma Phys.*, *12*, 705.

Gibson, S. E., D. L. Newman, and M. V. Goldman (1995), Langmuir turbulence and three-wave nonlinear dynamics, *Phys. Rev. E*, *52*, 558.

Ginzburg, V. L., and V. V. Zheleznyakov (1958), On the possible mechanisms of sporadic solar radio emission (radiation in an isotropic plasma), *Soviet Astron.*, *2*, 653.

Goldman, M. V., D. L. Newman, J. G. Wang, and L. Muschietti (1996), Langmuir turbulence in space plasmas, *Phys. Scripta*, *63*, 28.

Harvey, C. C., L. Celnikier, and D. Hubert (1988), Results from the ISEE propagation density experiment, *Adv. Space Res.*, *8*, 185.

Henri, P., C. Briand, A. Mangeney, S. D. Bale, F. Califano, K. Goetz, and M. Kaiser (2009), Evidence for wave coupling in type III emissions, *J. Geophys. Res.*, *114*, A03103, doi:10.1029/2008JA013738.

Hoang, S., G. A. Dulk, and Y. Leblanc (1994), Interplanetary type 3 radio bursts that approach the plasma frequency: ULYSSES observations, *Astron. Astrophys.*, *289*, 957.

Hospodarsky, G. B., and D. A. Gurnett (1995), Beat-type Langmuir wave emissions associated with a type III solar radio burst: Evidence of parametric decay, *Geophys. Res. Lett.*, *22*, 1161.

Huang, Y., and G.-L. Huang (2008), Solar type III bursts and the generation of backward Langmuir wave, *Chin. Astron. Astrophys.*, *32*, 178.

Intrator, T., C. Chan, N. Hershkowitz, and D. Diebold (1984), Nonlinear self-contraction of electron waves, *Phys. Rev. Lett.*, *53*, 1233.

Li, B., A. J. Willes, P. A. Robinson, and I. H. Cairns (2003), Dynamics of beam-driven Langmuir and ion-acoustic waves including electrostatic decay, *Phys. Plasmas*, *10*, 2748.

Lin, R. P., W. K. Levedahl, W. Lotko, D. A. Gurnett, and F. L. Scarf (1986a), Evidence for nonlinear wave-wave interactions in solar type III radio bursts, *Astrophys. J.*, *308*, 954.

Lin, R. P., W. K. Levedahl, W. Lotko, D. A. Gurnett, and F. L. Scarf (1986b), Evidence for nonlinear wave-wave interactions in solar type III radio bursts, *Astrophys. J.*, *308*, 954.

Lin, R. P., et al. (1995), A three-dimensional plasma and energetic particle investigation for the Wind spacecraft, *Space Sci. Rev.*, *71*, 125.

Mangeney, A., F. Califano, C. Cavazzoni, and P. Travnicek (2002), A numerical scheme for the integration of the Vlasov-Maxwell system of equations, *J. Comput. Phys.*, *179*, 495.

Matsukiyo, S., R. A. Treumann, and M. Scholer (2004), Coherent waveforms in the auroral upward current region, *J. Geophys. Res.*, *109*, A06212, doi:10.1029/2004JA010477.

Muschietti, L., I. Roth, and R. E. Ergun (1995), Kinetic localization of beam-driven Langmuir waves, *J. Geophys. Res.*, *100*, 17,481.

Muschietti, L., I. Roth, and R. E. Ergun (1996), On the formation of wave packets in planetary foreshocks, *J. Geophys. Res.*, *101*, 15,605.

Nishikawa, K. (1968), Parametric excitation of coupled waves. II. Parametric plasmon-photon interaction, *J. Phys. Soc. Jpn.*, *24*, 1152.

Omura, Y., H. Kojima, and H. Matsumoto (1994), Computer simulation of electrostatic solitary waves: A nonlinear model of broadband electrostatic noise, *Geophys. Res. Lett.*, *21*, 2923.

Omura, Y., H. Matsumoto, T. Miyake, and H. Kojima (1996), Electron beam instabilities as generation mechanism of electrostatic solitary waves in the magnetotail, *J. Geophys. Res.*, *101*, 2685.

Pedersen, A. (1995), Solar wind and magnetosphere plasma diagnostics by spacecraft electrostatic potential measurements, *Ann. Geophys.*, *13*, 118.

Robinson, P. A., A. J. Willes, and I. H. Cairns (1993), Dynamics of Langmuir and ion-sound waves in type III solar radio sources, *Astrophys. J.*, *408*, 720.

Sagdeev, R. Z., and A. A. Galeev (1969), *Nonlinear Plasma Theory*, Benjamin, New York.

Silin, I., R. Sydora, and K. Sauer (2007), Electron beam-plasma interaction: Linear theory and Vlasov-Poisson simulations, *Phys. Plasmas*, *14*, 012106.

Soucek, J., T. Dudok de Wit, V. Krasnoselskikh, and A. Volokitin (2003), Statistical analysis of nonlinear wave interactions in simulated Langmuir turbulence data, *Ann. Geophys.*, *21*, 681.

Sprague, R. A., and J. A. Fejer (1995), Simultaneous excitation of parametric decay cascades and of the oscillating two-stream instability in one-dimensional numerical simulations based on Zakharov's equations, *J. Geophys. Res.*, *100*, 23,959.

Umeda, T. (2007), Vlasov simulation of Langmuir wave packets, *Nonlinear Processes Geophys.*, *14*, 671.

Umeda, T., and T. Ito (2008), Vlasov simulation of Langmuir decay instability, *Phys. Plasmas*, *15*, 084503.

Usui, H., H. Furuya, H. Kojima, H. Matsumoto, and Y. Omura (2005), Computer experiments of amplitude-modulated Langmuir waves: Application to the Geotail observation, *J. Geophys. Res.*, *110*, A06203, doi:10.1029/2004JA010703.

C. Briand, F. Califano, P. Henri, and A. Mangeney, Laboratoire d'Études Spatiales et d'Instrumentation en Astrophysique, Observatoire de Paris, Université Pierre et Marie Curie, Université Paris Diderot, CNRS, 5 Pl. Jules Janssen, F-92190 Meudon, France.